



GIXSGUI: a MATLAB toolbox for grazing-incidence X-ray scattering data visualization and reduction, and indexing of buried three-dimensional periodic nanostructured films

Zhang Jiang*

Received 1 November 2014

Accepted 3 March 2015

X-ray Science Division, Argonne National Laboratory, Argonne, IL 60439, USA. *Correspondence e-mail: zjiang@aps.anl.gov

Edited by G. Renaud, CEA–Grenoble, France

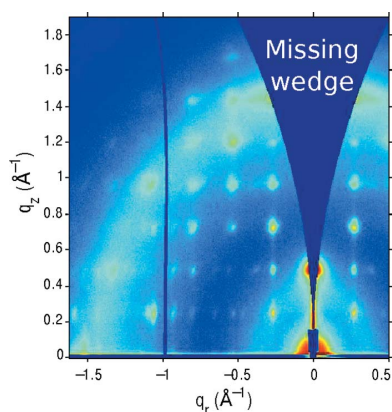
Keywords: grazing-incidence X-ray scattering; periodic nanostructured film; indexing.

GIXSGUI is a MATLAB toolbox that offers both a graphical user interface and script-based access to visualize and process grazing-incidence X-ray scattering data from nanostructures on surfaces and in thin films. It provides routine surface scattering data reduction methods such as geometric correction, one-dimensional intensity linecut, two-dimensional intensity reshaping *etc.* Three-dimensional indexing is also implemented to determine the space group and lattice parameters of buried organized nanoscopic structures in supported thin films.

1. Introduction

Grazing-incidence X-ray scattering (GIXS) is a surface probe for the study of nanostructures and nanocomposites at surfaces and in thin films. Because of the statistical sampling of the macroscopic area, ready adaptation for various *in situ* experimental environments and enhanced scattering signals at grazing angles as a result of total external reflection, GIXS in recent years has become a standard characterization technique applied for a variety of two-dimensional systems, ranging from Langmuir monolayers on liquid surfaces, and self-assembled block copolymer and nanoparticle films, to battery membrane layers and organic photovoltaic materials (Renaud *et al.*, 2009; Chen *et al.*, 2012; Müller-Buschbaum, 2014). GIXS experiments are often categorized into two regimes, depending on the dimension of the structure to be measured: grazing-incidence small-angle (GISAXS) and wide-angle (GIWAXS) X-ray scattering, with typical probing wavevector magnitudes (q) of 10^{-3} – 10^{-1} nm $^{-1}$ and 10^{-1} – 10 nm $^{-1}$, which translate to real-space length scales of 10 nm–1 μ m and 0.1 nm–10 nm, respectively.

While high surface sensitivity is a unique feature of GIXS, it makes the interpretation of the resulting data complicated. To obtain three-dimensional information, one needs to understand the scattering pattern in the reciprocal space in three orthogonal directions with respect to the sample surface and the forward direction of the incident beam (see §2.1.2). Quantitative analysis of the scattering at angles near the critical angle for total external reflection requires the theory of the distorted wave Born approximation (DWBA), which relies on the specific modeling of morphologies in individual samples. Because of the diversity and hierarchic nature of nanostructured materials, it is a challenge to perform a standard interpretation of GIXS data for all types of surface and thin-film samples. Among publicly released software, *IsGI-*



© 2015 International Union of Crystallography

SAXS is specialized for shape and correlation analysis of supported nano-islands (Lazzari, 2002); *FitGISAXS* is for supported or buried scatterers as well as interface roughness correlation (Babonneau, 2010); *BornAgain* is for particle shape and distribution analysis (<http://apps.jcns.fz-juelich.de/src/BornAgain/>); *HipGISAXS* is for simulating two-dimensional GISAXS patterns using parallel high-performance computing (Chourou *et al.*, 2013); *NANOCELL* is for simulating periodic continuous nanostructures in films (Tate *et al.*, 2006); *SimDiffraction* is for analyzing GIWAXS patterns of textured films (Breiby *et al.*, 2008); and the *DPC (Diffraction Pattern Calculator)* toolkit is for the identification of crystal unit-cell parameters from GIWAXS (Smilgies & Blasini, 2007; Hailey *et al.*, 2014). Nevertheless, most GIXS data analysis requires a general data reduction and analysis route before one proceeds to more detailed and quantitative modeling. For example, a facile method for extracting in-plane, vertical or azimuthal line profiles with respect to the surface can provide information about the size and orientation of the nanostructures that can both help guide experimental protocols and provide a bridge between experimental data and more detailed analysis. More often, the symmetry of periodic nanostructures in thin films in terms of lattice spacing, orientation and space group can be identified from GIXS experiments. For these purposes, *GIXSGUI*, a package based on MATLAB (The MathWorks Inc., Natick, MA, USA), was developed for GIXS data visualization and processing, as well as three-dimensional nanostructure indexing.

2. GIXSGUI design and capability

The toolbox is designed with a graphical user interface (GUI), which is based on the MATLAB handle class data type *gixsdata*. Data and experiment parameters are input and stored as properties of *gixsdata*, and data operations are achieved via the built-in methods of *gixsdata* (see Appendix A for a list of key properties and methods, and the software manual downloadable with the toolbox for a comprehensive description and usage). This design also allows a script mode fully independent of the GUI, enabling batch processing and data automation for the large data sets that often result from *in situ* and time-resolved experiments.

2.1. Flow of GIXS data processing

2.1.1. Data corrections. *GIXSGUI* supports typical GIXS experimental data in which a two-dimensional area detector is fixed at a stationary position with the direct incident beam impinging normal to the detector face. Obtaining the differential scattering cross section of the sample requires a number of data corrections on the two-dimensional GIXS pattern to account for detection efficiency, flat-field incident X-ray polarization, solid-angle variation, the Lorentz effect *etc.*

Efficiency correction needs to account for two factors: medium (e.g. air) path attenuation and detector sensor absorption. Both corrections are especially crucial for experiments with an ultra-short sample-to-detector distance,

e.g. GIWAXS. Pixels at larger oblique angles 2θ have a larger sample-to-pixel distance and therefore a larger medium attenuation (Fig. 1). This effect can be corrected by multiplying the measured intensity by

$$E_m = 1/[\exp(-\mu_m \text{SDD}/\cos 2\theta)], \quad (1)$$

in a pixel-by-pixel manner, where μ_m is the linear mass attenuation coefficient of the path medium, SDD is the nominal sample-to-detector distance with respect to the direct beam pixel and 2θ is the oblique scattering angle. E_m is unity for measurements conducted in a vacuum environment all the way from the sample to the detector. However, the vacuum setup is usually inconvenient for GIWAXS, or may be incompatible for *in situ* investigations. On the other hand, the detector sensor absorption correction is due to the variation of X-ray absorption probabilities across pixels and depends on the properties of the detector. For direct-detection pixel-array detectors such as Pilatus (Dectris Inc.), X-rays impacting at different oblique angles result in different path lengths in the detector sensor. The probability of stopping and detecting X-ray photons increases as the angle increases. The correction is given by

$$E_d = 1/[1 - \exp(-\mu_d t_d/\cos 2\theta)], \quad (2)$$

where μ_d is the linear mass attenuation coefficient of the sensor material and t_d is the thickness of the sensor plate. The efficiency correction is optional depending on the experiment setups and detector types.

Flat-field correction removes artifacts that are caused by variations in the pixel-to-pixel sensitivity of the detector. *GIXSGUI* achieves this by multiplying each image on a pixel-by-pixel basis with a normalized pre-calibrated two-dimensional image provided by the detector manufacturer.

GIXS data collected at synchrotron-based facilities have to be adjusted for the polarization effect. Typical synchrotron radiation is linearly polarized in the horizontal plane (except for certain types of synchrotron sources, such as the elliptical polarizing undulator source), causing reduced observed scattering intensity at smaller ψ angles (the angle between the polarization and the exit wavevector \mathbf{k}_f) (Fig. 2). The correction for horizontal polarization is given by

$$P_h = |\sin \psi|^2 = 1 - \cos^2 \delta \sin^2 \gamma. \quad (3)$$

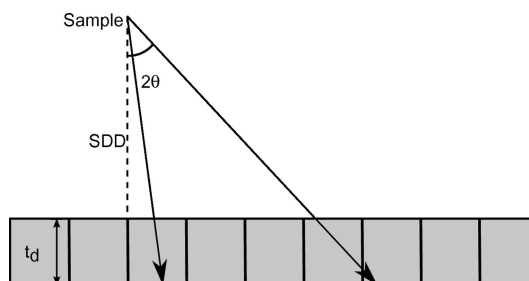


Figure 1
Photons scattered to larger oblique angles are more attenuated in the path medium and have increased absorption probability in the detector sensor.

GIXSGUI implements three more types of polarization correction. For a vertically polarized source, $P_v = \cos^2 \delta$. For a horizontally or vertically polarized source with partial polarization, $P_p = \zeta P_h + (1 - \zeta) P_v$, where $\zeta \in [0, 1]$ is the fraction of the radiation that is polarized in the horizontal direction. $\zeta \simeq 98\%$ for most synchrotron-based GIXS experiments. For an unpolarized source, $P_u = \frac{1}{2}(P_h + P_v) = \frac{1}{2}(1 + \cos^2 2\theta)$.

The measured intensity on a pixel is proportional to the solid angle subtended by that pixel and needs to be normalized with respect to a reference, *e.g.* the solid angle of the direct beam pixel. Solid-angle correction is needed purely to account for a geometric effect that applies to all types of detector and is given by

$$C_s = \Delta\Omega_0 / \Delta\Omega_i, \quad (4)$$

where $\Delta\Omega_0$ and $\Delta\Omega_i$ are the solid angles of the direct beam and the *i*th pixel, respectively.

Lorentz correction is usually used to correct the intensities of X-ray scattering of single-crystal diffractometry in order to obtain the real intensities for structure factors. Many single-crystal diffraction experiments have been and are performed by spinning the crystal along an axis. Therefore one needs to correct for the differences of the time that individual reciprocal lattice points spend on the surface of the Ewald sphere. A similar scenario applies to powders whose orientational randomness is in a given plane. One can calculate the Lorentz correction factor by deriving the Jacobian for the transformation of the integration volume (over the differential scattering cross section) from the angular expression to the $d\mathbf{h}d\mathbf{k}d\mathbf{l}$ expression in the reciprocal space (Vlieg, 1997), or alternatively by the Buerger precession method (Buerger, 1940). For example, the Lorentz factor L for an ω scan is proportional to the velocity of the diffraction spot P leaving the Ewald sphere surface (Fig. 3) so that

$$L_{hkl} \simeq \frac{1}{S} \frac{1}{\sin 2\theta}, \quad (5)$$

where the level-scale factor $S = \cos \alpha_i \cos \alpha_f$ for three-dimensional powders randomly oriented on the sample surface plane around the surface normal axis. S is constant for a given level l but is different for different experimental geometries and

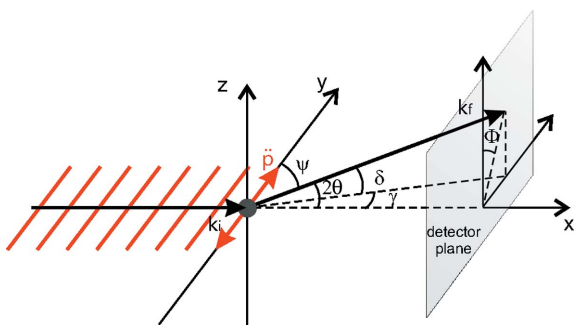


Figure 2

Electrons in a sample become dipoles oscillating along the direction of the polarization of the incident wave, resulting in less observed scattered intensity at smaller ψ angles. The geometry is in the laboratory reference frame.

samples. For a two-dimensional sample whose grains are randomly oriented on the sample surface, $S = 1$. For a completely randomly oriented sample, the scattering depends only on the oblique angle 2θ (see Fig. 2) and the Lorentz factor $L \simeq 1/(4 \sin^2 \theta \cos \theta)$ (Cullity & Stock, 2001), which is often used for bulk samples measured in a transmission geometry such as SAXS and WAXS. For a single crystal that constantly rotates across its Bragg angle, the Lorentz factor is written as $L \simeq 1/\sin 2\theta_{\text{Bragg}}$ (Reynolds, 1986; Als-Nielsen & McMorrow, 2011). A Lorentz correction should only be applied to scattering from lattices where there is periodicity with a great number of repeating scattering units. Inappropriately applying a Lorentz correction to scattering from individual particles destroys the characteristics of the scattering curve (*e.g.* it falsely reduces the intensity of the form factor to zero near the zero scattering angle and also produces an artificial maximum at a nonzero scattering angle) (Cser, 2001). A few types of Lorentz factor are built in to *GIXSGUI*, but users should be aware that, although the correction is performed on the entire image for convenience, only the intensities on pixels representing periodic structures (*i.e.* structure factors) should be corrected. For sample orientations or geometries not listed in *GIXSGUI*, one may apply a corresponding correction factor later to one-dimensional line profiles. For example, the specular rod (00*l*) for which the in-plane scattering angle $2\theta = 0$ and the rocking scan angle is the incident angle α requires a Lorentz factor of $L \simeq 1/\sin 2\alpha$ (Smilgies, 2002; Shayduk, 2010).

A number of other corrections that may need to be considered include sample absorption, resolution for beam divergence and energy dispersion, footprint correction for illumination area, and intensity integration of the interception of the scattering rod for surface diffuse scattering analysis (Vlieg, 1997, 1998; Robach *et al.*, 2000; Smilgies, 2002, 2009; He, 2009). Depending on the sample specifics (*e.g.* size, shape and thickness), experimental configuration and requirements

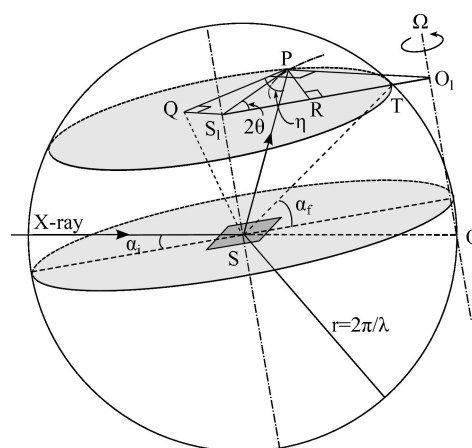


Figure 3

The Buerger precession method for the Lorentz factor for an ω scan is illustrated with the help of the Ewald sphere. For a lattice point P which rotates around the surface normal axis OO_i at a constant angular velocity Ω , the Lorentz factor L_{hkl} is inversely proportional to its velocity of leaving the Ewald sphere surface $V_{hkl} = \Omega \mathbf{PO}_i \cos \eta$. Simple geometric calculations lead to $L_{hkl} \simeq 1/(\cos \alpha_i \cos \alpha_f \sin 2\theta)$.

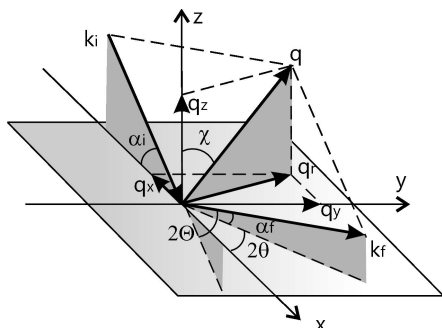


Figure 4
Schematic diagram of grazing-incidence scattering geometry in the sample reference frame.

for data analysis, not every correction is needed. For example, one would expect the path of X-rays traveling underneath the surface to be longer for lower exit angles, which implies a larger absorption. However, in many thin films the sample absorption is negligibly small and can therefore be omitted (Baker *et al.*, 2010). With the intensities and reciprocal map values (*i.e.* angles and q values) of each pixel accessible in *gixsdata*, one can apply customized corrections to the entire image (through a customized correction matrix C_c in *gixsdata*) or, more conveniently, later to line profiles during the data modeling and fitting procedures.

Scattering intensity distortion at grazing incident and exit angles, *e.g.* surface scattering enhancement and waveguide mode, is a unique feature of surface scattering geometries. It needs to be taken into account but cannot be eliminated straightforwardly by multiplying a correction coefficient with the raw GIXS data. As a dynamic scattering effect, it can only be treated with proper surface scattering theories such as the DWBA (see §2.2). In fact, one can take advantage of this effect to probe the surface or bulk selectively and obtain depth-dependent structures with extraordinarily high resolution (Wang *et al.*, 1991, 1992; Jiang *et al.*, 2011), rather than treating it as a troublesome correction.

2.1.2. Scattering geometry. The convention adopted by *GIXSGUI* for grazing-incidence scattering geometry is illustrated in Fig. 4, where \mathbf{k}_i and \mathbf{k}_f are the incident and exit wavevectors, α_i and α_f are the incident and exit angles, and 2θ is the in-plane scattering angle. Normal and in-plane components of the wavevector transfers for each pixel (q maps) are calculated in the sample frame by

$$q_z = k_f \sin \alpha_f + k_i \sin \alpha_i, \quad (6)$$

$$q_x = k_f \cos \alpha_f \cos 2\theta - k_i \cos \alpha_i, \quad (7)$$

$$q_y = k_f \cos \alpha_f \sin 2\theta, \quad (8)$$

$$q_r = (q_x^2 + q_y^2)^{1/2}. \quad (9)$$

In *gixsdata*, the maps are computed by the method *qmaps*, which first computes the exit angle α_f and out-of-plane angle 2θ using the experimental parameters (energy, incident angle, direct beam position, pixel sizes, specular beam position *etc.*).

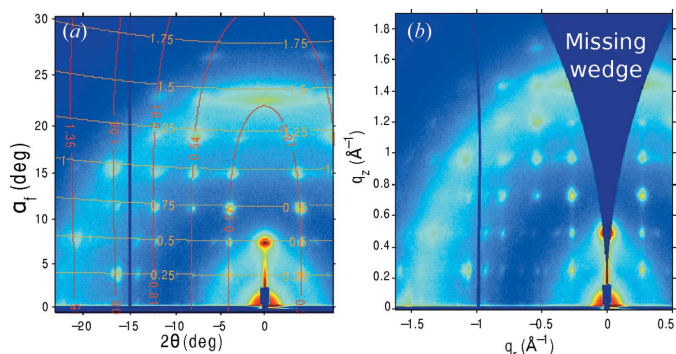


Figure 5
GIWAXS pattern (a) before and (b) after reshaping with respect to q_z and q_r , whose contour lines are shown in gold and red in (a).

The full q maps are then calculated according to equations (6)–(9).

2.1.3. Linecut and image reshape. With the built-in *linecut* method, one can reduce two-dimensional GIXS data into one-dimensional profiles with respect to any angle or q components, prior to further structure modeling (such as for lattice parameter, nanostructure size and shape analysis) with functions either integrated with the MATLAB curve fitting toolbox or developed by users for specific purposes. See §2.4 for an example.

The measured intensity distribution on an area detector does not directly represent the sample's reciprocal space, *i.e.* the q maps on the detector are not orthogonal for the natural arrangement of the pixel arrays. Rather, one measures the projection of the reciprocal lattice intercepted by the Ewald sphere onto the detector plane. To do analyses such as for crystalline orientation and texture, one can either use the one-dimensional profiles as a function of angle obtained directly with *linecut* or, more conveniently, reconstruct the GIXS image to one represented by orthogonal reciprocal space axes (*e.g.* in q_z and q_r , or in q_z and χ , where χ is the polar angle of the reciprocal space¹). For example, Fig. 5(a) shows a raw GIWAXS pattern from a thin film of conjugated block copolymers, which self-assemble into two-dimensional powder-like nanostructures in the film plane. The contours of the constant out-of-plane and in-plane wavevector transfers, q_z and q_r , respectively, in the raw scattering pattern do not follow the columns and rows of pixels and are not orthogonal to each other, especially at high exit and in-plane scattering angles. Reshaping with the built-in method *reshape_image* redistributes the intensities into the natural reciprocal space coordinates of the sample (Fig. 5b). The reshaping is a simple two-dimensional image transformation that is performed in a backward manner, *i.e.* for each pixel in the reshaped image of a user-preset reshaping resolution (*i.e.* step or pixel size), *gixsdata* looks backwards within the original intensity-corrected image for pixels that fulfill the boundary conditions (*i.e.* angle or q constraints) for the new pixel and calculates the

¹ In contrast to Φ , the polar angle of the detector plane (Fig. 2), χ is the polar angle of the reciprocal space with respect to the surface normal, *i.e.* the angle between the q_z direction and \mathbf{q} (Fig. 4). Crystalline and texture orientation analysis is often done by analyzing the intensity distribution in terms of χ .

mean intensity of those pixels. It is noted that, owing to the refraction–reflection effects, the q or angle (especially q_z or α_f) space representing the buried sample structures distorts and splits into multiple peak sets (§2.2). In addition, the interference arising from the multiple interfaces causes the so-called waveguide or standing-wave effect and induces significant distortion in the scattering intensity distribution near the critical angles of the film and the substrate (Wang *et al.*, 1991, 1992; Jiang *et al.*, 2011). As discussed in §2.1.1, these effects cannot be straightforwardly accounted for during image reshaping. However, these effects are usually diminished as the angles increase beyond (typically at least $2\text{--}3\times$ larger than) the critical angles. Therefore, image reshaping is more frequently performed for GIWAXS and GIXD patterns. After reshaping a single GIXS image, a blank region (also termed a missing wedge) appears, as shown in Fig. 5(b), which is the q space that cannot be probed at a fixed incident angle (Breiby *et al.*, 2008; Baker *et al.*, 2010; Liao *et al.*, 2013). This often causes a problem for crystalline orientation analysis with respect to the film surface using Bragg diffraction on the q_z axis. It then leads to a general problem of determining comprehensive structures and lattice parameters for crystals. This problem can be solved by the technique of reciprocal space mapping (Pereira *et al.*, 2002; Smilgies *et al.*, 2005; Yoshida *et al.*, 2007), which transforms a set of angular scans taken with slightly different offsets into a reconstructed two- or three-dimensional reciprocal space. In this example, one can collect a series of images by scanning the incident angle near the Bragg angle to patch up the missing wedge, so-called pole figure construction (Baker *et al.*, 2010).

2.2. Three-dimensional nanostructure indexing

GIWS is nowadays routinely performed to solve for the nanoscale crystalline structures in assembled thin films consisting of nanoparticles, macromolecules and their composite materials. Three-dimensional nanostructure indexing is in high demand for fast characterization of the morphology and quality of the assembly in these films. The indexing method is slightly different from that applied in traditional crystallography on powders, owing to the refraction and reflection effects in the presence of interfaces (*e.g.* film–air and film–substrate). Electron-density contrasts at interfaces induce angle changes on both the incident and exit sides (as shown at the top interface in Fig. 6). The amount of angle change can be calculated *via* Snell's law (Als-Nielsen & McMorrow, 2011; Tolan, 1999). On the other hand, the reflection from the substrate surface effectively flips the directions of the incident and scattered beams. These two effects are combined, leading to a split of the diffraction and a distortion of the reciprocal space that are commonly seen in grazing-incidence experiments.

In the framework of the DWBA for buried structures (Sinha *et al.*, 1988; Rauscher *et al.*, 1999; Lazzari, 2002; Lee, Park, Yoon *et al.*, 2005; Busch *et al.*, 2006; Tate *et al.*, 2006; Stein *et al.*, 2007; Jiang *et al.*, 2011), the differential scattering cross section is given by

$$\left(\frac{d\sigma}{d\Omega}\right)_{\text{diff}} \simeq r_e^2 |\Delta\rho|^2 |\mathcal{F}(q_r, k_{z,1}^i, k_{z,1}^f)|^2, \quad (10)$$

where r_e is the Thompson scattering length of an electron, $\Delta\rho$ is the electron density contrast of the nanostructures in the film, $k_{z,1}^i$ and $k_{z,1}^f$ are the z components of the incident and exit wavevectors in medium 1 (the subscript 1 is often dropped for convenience) above the film (*e.g.* air or vacuum), respectively, and

$$\begin{aligned} \mathcal{F}(q_r, k_{z,1}^i, k_{z,1}^f) = & T_2(k_{z,2}^f) T_2(k_{z,2}^i) F(q_r, q_{z,2}^1) \\ & + R_2(k_{z,2}^f) T_2(k_{z,2}^i) F(q_r, q_{z,2}^2) \\ & + T_2(k_{z,2}^f) R_2(k_{z,2}^i) F(q_r, q_{z,2}^3) \\ & + R_2(k_{z,2}^f) R_2(k_{z,2}^i) F(q_r, q_{z,2}^4). \end{aligned} \quad (11)$$

Here, F is the Fourier transform of the electron-density variation in the film, and $|F|^2$ can be viewed as the structure factor of a periodic lattice (to be solved for by three-dimensional indexing), or simply as a form factor in the case of dilutely distributed objects. The four terms in equation (11) have clear physical meaning and represent four scattering events (see Fig. 6) as a result of refraction at the film surface, reflection at the film/substrate interface and diffraction by the nanostructure. Each term is weighted by combinations of the incident and exit wavevector-dependent (*i.e.* angle-dependent) T_2 and R_2 , which are the complex amplitudes of the transmitted and reflected waves in medium 2 (film) and can be calculated by Parratt's recursion method (Parratt, 1954; Tolan, 1999). The z components of the wavevector transfer of the four events are given by, respectively,

$$\begin{aligned} q_{z,2}^1 &= k_{z,2}^f - k_{z,2}^i, \\ q_{z,2}^2 &= -k_{z,2}^f - k_{z,2}^i, \\ q_{z,2}^3 &= k_{z,2}^f + k_{z,2}^i, \\ q_{z,2}^4 &= -k_{z,2}^f + k_{z,2}^i. \end{aligned} \quad (12)$$

Here, $k_{z,2}^i = k_2 \sin \alpha_2^i$ and $k_{z,2}^f = k_2 \sin \alpha_2^f$ (with k_2 the wave-vector amplitude of the X-ray in medium 2) are the z components of the incident and exit wavevectors in medium 2, respectively, and can be determined *via* Snell's law $\cos \alpha_1^{(i,f)} = n_2 \cos \alpha_2^{(i,f)}$ (with n_2 the index of refraction in

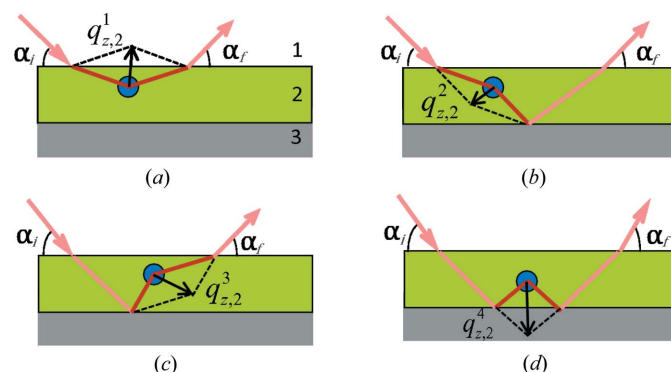


Figure 6
Schematic of the four scattering events inside a supported film as a result of the combination of refraction, diffraction and reflection.

medium 2). At a fixed incident angle, scattering for a given wavevector transfer (q_z, q_r) may exit the film surface at two angles because of refraction and reflection effects,

$$\alpha_f = \arcsin \left[\left(\frac{q_z}{k} \right)^2 + \sin^2 \alpha_i \mp \frac{2q_z}{k} (n^2 - 1 + \sin^2 \alpha_i)^{1/2} \right]^{1/2}, \quad (13)$$

where the $-$ channel is for terms 1 and 2, and the $+$ channel is for terms 3 and 4 in equation (11), respectively. The in-plane scattering angle is

$$2\theta = \arccos \left[\frac{\cos^2 \alpha_f + \cos^2 \alpha_i - (q_r/k)^2}{2 \cos \alpha_f \cos \alpha_i} \right]. \quad (14)$$

As implied in Figs. 6(a) and 6(b), the $-$ channel occurs with the incident beam directly scattered from the structure without first being reflected from the substrate and is therefore named the transmission channel. Correspondingly, in Figs. 6(c) and 6(d), the $+$ channel occurs with the incident beam reflected from the substrate before scattering and is therefore named the reflection channel.

When the Laue condition $\mathbf{q} = \mathbf{G}$ is fulfilled (where \mathbf{G} are the reciprocal lattice vectors of the nanostructures), diffraction can be observed in the transmission and reflection channels whose exit angles can be obtained through Ewald sphere construction described as follows. The Ewald sphere is defined in the laboratory frame (coordinate system defined in Fig. 2), whereas the reciprocal space is conveniently defined in the sample frame (coordinate system defined in Fig. 4). The two frames are related by an incident-angle-dependent rotation matrix

$$R_y(\alpha_i) = \begin{bmatrix} \cos \alpha_i & 0 & \sin \alpha_i \\ 0 & 1 & 0 \\ -\sin \alpha_i & 0 & \cos \alpha_i \end{bmatrix}. \quad (15)$$

The reciprocal lattice vector in the laboratory frame is then rewritten as

$$\mathbf{G}_{\text{lab}} = (G_x, G_y, G_z) = R_y \mathbf{G}_{\text{sample}} = R_y (h\mathbf{a}_1^* + k\mathbf{a}_2^* + l\mathbf{a}_3^*), \quad (16)$$

where (h, k, l) are Miller indices and $(\mathbf{a}_1^*, \mathbf{a}_2^*, \mathbf{a}_3^*)$ are the reciprocal space basis vectors. The Laue condition requires that the lattice points fall on the Ewald sphere surface in order to be observed,

$$|\mathbf{G}_{\text{lab}} - \mathbf{k}|^2 - |\mathbf{k}|^2 = (G_x - k)^2 + G_y^2 + G_z^2 - k^2 \leq \Delta G^2, \quad (17)$$

where ΔG accounts for the finite size of the diffraction in the reciprocal space and any mosaicity of the domains.

The domains of substrate-supported nanostructures often have a statistically distributed orientation with respect to the surface normal. If the orientation is isotropic in the plane, which is the case for most self-assembled structures on flat substrates, the reciprocal lattice becomes a set of q_r -dependent rings (two-dimensional powder rings). Therefore, \mathbf{G}_{lab} fulfilling the Laue condition is related to the wavevector transfer (q_x, q_y, q_z), which is defined in the sample frame by

$$G_x^2 + G_y^2 + G_z^2 - q_r^2 + q_z^2 + q_z(G_x \sin \alpha_i - G_z \cos \alpha_i) = 0 \quad (18)$$

and

$$-G_x \sin \alpha_i + G_z \cos \alpha_i = q_z. \quad (19)$$

The diffraction angles from nanostructures of a given lattice type and parameters are then calculated by substituting (q_r, q_z) values obtained by simultaneously solving equations (17)–(19) into equations (13) and (14).

In a diffraction pattern, all those symmetric extinctions or absences can be traced back to the symmetry elements that have caused them, providing a very useful method for space-group identification. In *GIXSGUI*, one can calculate the diffraction positions of any of the 230 space groups and superimpose them over the experimental GIXS patterns to determine the space group of the sample. For simple lattices, one can straightforwardly construct the unit cell by assigning the fractional basis coordinates. See examples in §2.4 for details.

2.3. Other features

GIXSGUI supports a variety of GIXS data image formats, including TIF (TIFF), MAT (MATLAB), CBF (crystallographic binary file), FITS (flexible image transport system) and EDF (European data format), and can easily be extended to other formats. It integrates the surface tilt-angle correction to account for the tilt during sample mounting. The sample-to-detector distance can be calibrated using either a silver behenate ($\text{AgC}_{22}\text{H}_{43}\text{O}_2$) standard or specular reflections from a thin film or flat wafer (usually silicon) at multiple incident angles. *GIXSGUI* also allows users to customize image masks for data inclusion or exclusion. A number of other built-in methods and functions provided in the toolbox are accessible in script mode and can be flexibly adapted to the user's needs. They include, for example, *roicount* and *roiscan* for extracting the integrated intensity over a user-defined region of interest (ROI) for a series of two-dimensional image scans, and *gixs-diffpos* combined with *findpeak* and the MATLAB Optimization Toolbox for indexing three-dimensional structures in thin films. Detailed instructions on using these methods can be found in the software documentation.

Detailed data modeling depends on the desired level of structure information analysis and can vary significantly from sample to sample. While some models, such as particle shape and orientation analysis and film porosity analysis, have been discussed extensively (Lazzari, 2002; Lee, Park, Hwang *et al.*, 2005; Baker *et al.*, 2010) and implemented in a few analysis software distributions as listed in §1, others, for example in the presence of X-ray standing waves (Wang *et al.*, 1991, 1992; Jiang *et al.*, 2011), cannot be easily generalized and have to be developed for customized problems on an individual basis.

2.4. Case studies

Now we will employ a few examples to illustrate briefly how one can use *GIXSGUI* to reduce line profiles for lattice

parameter and nanostructure dimension analysis and use its three-dimensional indexing capability to solve for the space groups of nanoscale periodic structures.

Fig. 7(a) is GISAXS pattern from a silicon-supported film of spherical gold nanoparticles ordered in a two-dimensional superlattice. The superlattice is prepared *via* droplet evaporation of a colloidal suspension in toluene, in which the nanoparticles self-assemble into a monolayer superlattice at the interface (Narayanan *et al.*, 2004; Jiang *et al.*, 2010). With reciprocal space q maps automatically assigned in *GIXSGUI*, the q_y values at the two-dimensional Bragg peaks (vertical rods) were found to scale as $1:3^{1/2}:2:7^{1/2}$, indicating a two-dimensional hexagonal close-packed lattice. For further analysis, the line profile along q_y (Fig. 7b) was obtained by the *linecut* method and passed directly to the MATLAB Curve Fitting Toolbox (license required) to fit a Lorentzian function for the lattice parameter (from peak position) and coherent domain size (from the full width at half-maximum using the Scherrer relation). These are found to be 74.8 and 1122.0 Å, respectively. The line profile along q_z (Fig. 7c) usually reveals the structure in the direction normal to the film. In this case, the profile was fitted to a function in the framework of the DWBA (Jiang *et al.*, 2011) to analyze the nanoparticle size and polydispersity, which were found to be $R = 27.3$ Å and $\sigma_R = 2.6$ Å, respectively.

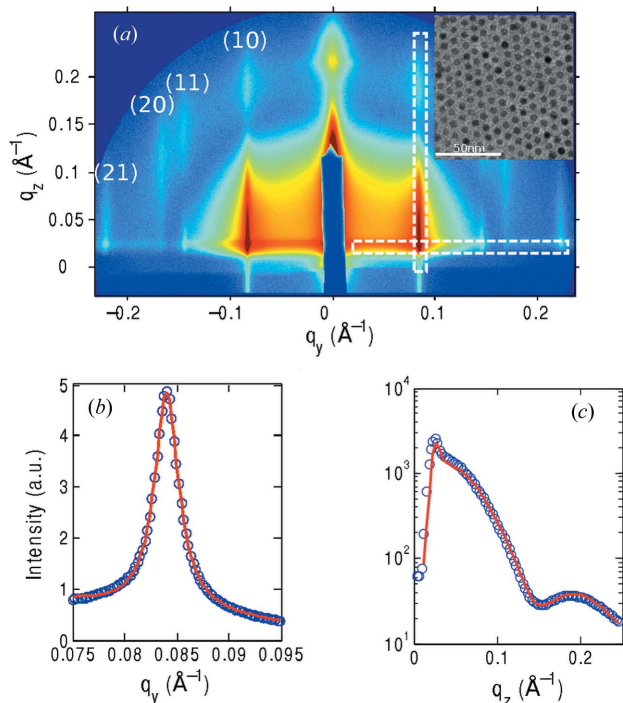


Figure 7

(a) GISAXS pattern from a film of gold nanoparticles in a monolayer superlattice taken with 7.35 keV X-rays incident at 0.18° . The inset shows a TEM image of the monolayer. (b) and (c) are linecuts along the q_y and q_z directions obtained by integrating the intensities in the white dashed boxes shown in part (a). Solid lines are best fits to (b) a Lorentzian function with the MATLAB Curve Fitting Toolbox for in-plane lattice parameters and (c) the multilayer DWBA theory developed following Jiang *et al.* (2011) for nanoparticle size and polydispersity.

The diffraction pattern in Fig. 8(a) arises from a self-assembled thin film of spherical gold nanoparticles blended in block copolymer (BCP)-based supermolecules [poly(styrene)-block-poly(4-vinylpyridine)-(3-pentadecylphenol)], or PS-*b*-P4VP(PDP), for short, with the subscript r being the ratio of PDP to 4VP units) (Kao *et al.*, 2012). After solvent annealing under chloroform, with the help of the assembly of PS(19)-*b*-P4VP(5.2)(PDP)_{1.7}, Au nanoparticles (6 vol.% loading) diffused into the dented rectangular interstitial sites among the PS cylinders (parallel to the film surface, but the grain orientations are random in the plane) to form nanoparticle chains. X-rays of 7.35 keV were incident on the sample surface at a grazing angle of 0.23° . The diffraction peaks are best calculated by assuming a rectangular centered lattice of cylinders parallel to the film surface, which can be constructed as a nonprimitive unit cell with lattice parameters $a = 330$ Å, $b = 425$ Å, $c = \infty$, $\alpha = \beta = \gamma = 90^\circ$, basis fractional coordinates

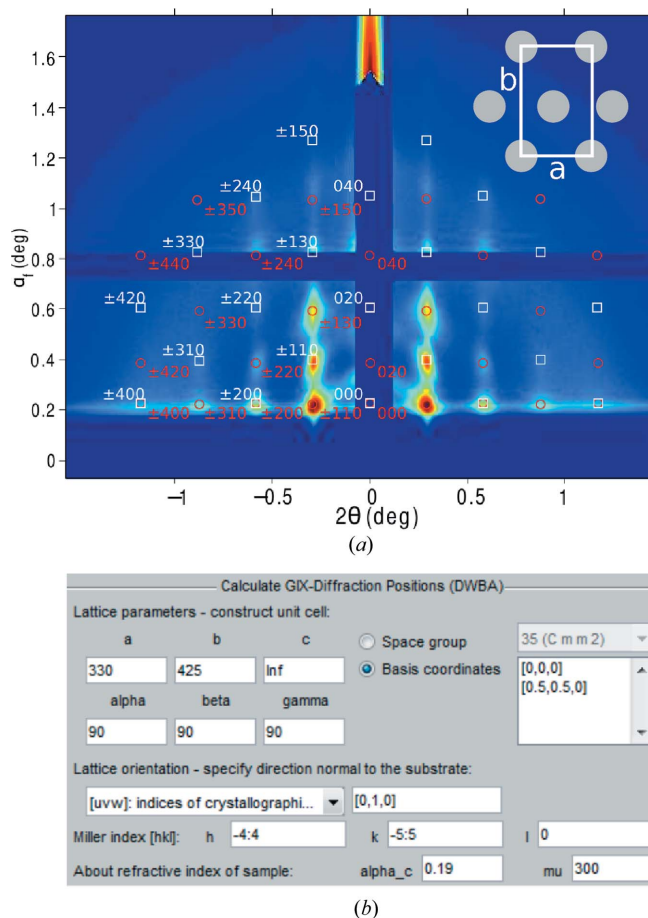


Figure 8

(a) GISAXS pattern from a film of gold-nanoparticle-loaded block-polymer-based supermolecular nanocomposites. The inset is a schematic view of the film's cross section, showing a rectangular centered lattice consisting of PS cylinders and nanoparticle chains parallel to the film surface. Red circles and white squares labeled with Miller indices are calculations using the lattice parameters (units: Å and $^\circ$), unit-cell orientation and averaged index of refraction of the film in terms of the critical angle (units: $^\circ$), and linear absorption coefficient (units: cm^{-1}) given in (b) (screenshot of *GIXSGUI*) for the transmission and reflection channels, respectively. Space group No. 35 *Cmm2* and the manually constructed unit cell both give identical calculations of the diffraction peaks.

$[0, 0, 0]$, $[\frac{1}{2}, \frac{1}{2}, 0]$, and $[uvw] = [010]$ (b axis) perpendicular to the film. Since the cylinders pack into a two-dimensional pattern (the cross section of the film is alike everywhere) of point group $mm2$, one can alternatively use space group No. 35 $Cmm2$ to calculate the diffraction pattern. In Fig. 8(a), note that two diffraction sets (white for reflection and red for transmission channels) appear as a result of the refraction and reflection effects, although they arise from the same structure. The extent of the vertical separation of the two channels depends on the difference of the incident angle above the critical angle, whereas they usually merge when the incident angle is less than the critical angle. One should therefore be careful during structure indexing on a GIXS pattern in order to avoid assigning the two channels to different lattice planes.

Fig. 9(a) shows the GISAXS pattern from a drop-cast thin film of Au nanoparticles encapsulated in micelles of cetyltrimethylammonium bromide (CTAB), an ionic surfactant. In the presence of silica precursors, the Au nanoparticle–micelle film self-assembles into a rhombohedral lattice whose grains are randomly oriented on the surface like a two-dimensional powder (Dunphy *et al.*, 2008). The diffraction peak positions were best calculated on the basis of a primitive rhombohedral lattice (space group No. 166 $R\bar{3}m$ using rhombohedral axes) with lattice parameters $a = b = c = 89$ Å, $\alpha = \beta = \gamma = 60^\circ$ and the $[111]$ direction normal to the film surface. A rhombohedral lattice with 60° lattice angles indicates an ideal close packing of ABCABC... type and enhances the symmetry to space group No. 216 $F\bar{4}3m$, *i.e.* an alternative lattice interpretation with a primitive face-centered cubic unit cell of $a = b = c = 126$ Å, $\alpha = \beta = \gamma = 90^\circ$ and $[uvw] = [111]$ normal to the film surface. While the calculated diffraction peak positions of these two lattice definitions are identical, the Miller indices are different because of the different choices of lattice interpretation (Fig. 9b).

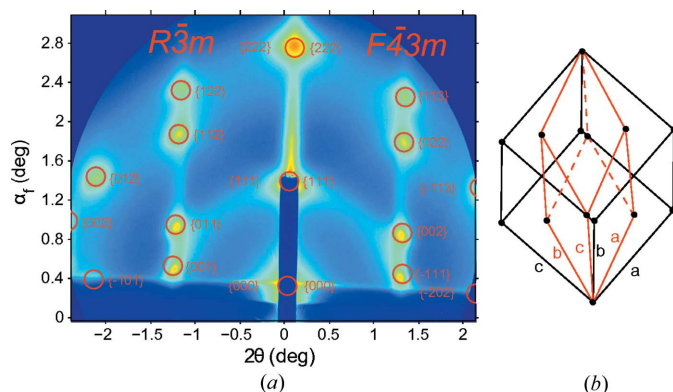


Figure 9
(a) GISAXS pattern from a composite thin film of self-assembled Au nanoparticle–CTAB micelles in the presence of silica precursors. The diffraction peaks are calculated using either a primitive rhombohedral unit cell ($R\bar{3}m$) or a face-centered cubic unit cell ($F\bar{4}3m$), with their corresponding diffraction plane indices labeled on the left and right sides of the GISAXS pattern, respectively. {} means the equivalence of h, k and l . The reflection and transmission channels merge because the incident angle is chosen exactly at the critical angle. For clarity, only one channel is displayed. View (b) illustrates the equivalence of the two lattice interpretations. For both, the $[111]$ direction is normal to the surface.

3. Distribution

GIXSGUI was developed for users at the dedicated GIXS beamline at Sector 8-ID-E, Advanced Photon Source (APS) (Jiang *et al.*, 2012), and it can be readily applied to GIXS data collected at other synchrotron facilities, as well as laboratory-based instruments. The package is actively maintained at the beamline, with new features constantly implemented in response to users' requirements. The most up-to-date distribution is available for free download at <http://www.aps.anl.gov/Sectors/Sector8/Operations/GIXSGUI.html>. The package is delivered with documentation for installation and usage instructions, as well as a set of commented examples for exercises.

APPENDIX A

List of key properties and methods of MATLAB class *gixsdata* and other functions in *GIXSGUI*

Key properties:

Camera, PixelSize, Beam0, SDD, XEnergy, Geometry, IncidentAngle: experimental conditions.

PolarizationMode, LorentzFactorType, FlatField, EfficiencyCorrection, CustomCorrection: corrections to the raw data.

RawData: uncorrected image data.

QMap, QxMap, QzMap, QyMap, QrMap, TwoThetaMap, AlphaMap, ChiMap and PhiMap: q and angle values for each pixel.

SolidAngleCorrectedData: image data after all corrections performed on a pixel-by-pixel basis.

$$I_{\text{corrected}} = I_{\text{raw}} \frac{E_m E_d F C_s C_c}{PL}, \quad (20)$$

where I_{raw} represents the raw data, E_m and E_d are the medium and detector efficiency corrections, F is the flat-field correction, C_s is the solid angle correction, C_c is a custom correction, P is the polarization correction and L is the Lorentz correction.

Key methods:

gixsdata: creates a new *gixsdata* object and returns the object handle.

qmaps: calculates q and angle maps.

imagesc: scales and displays image data.

linecut: performs a line cut.

reshape_image: converts the image into a user-defined Cartesian coordinate system.

findpeak: finds two-dimensional diffraction peak positions.

Other key functions:

gixsdifpos: calculates the grazing-incidence X-ray diffraction positions of polycrystalline films.

roiscan: extracts integrated intensity of a user-defined ROI over a set of images.

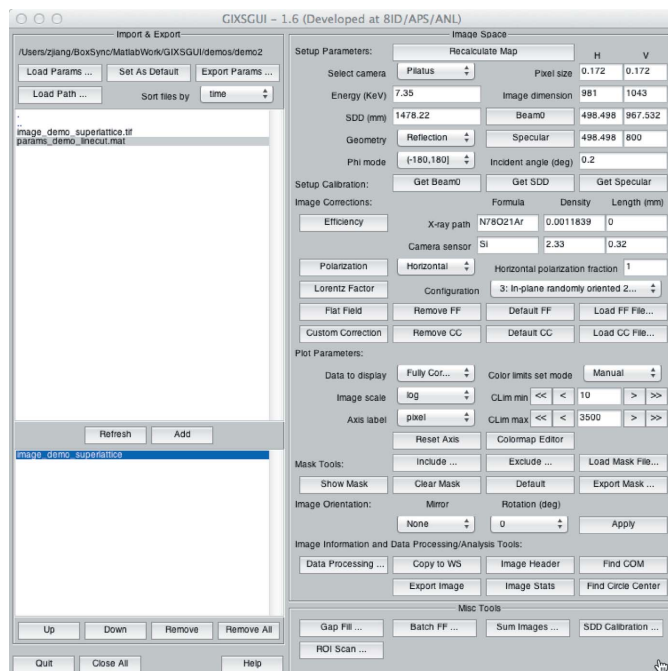


Figure 10
Main control panel.

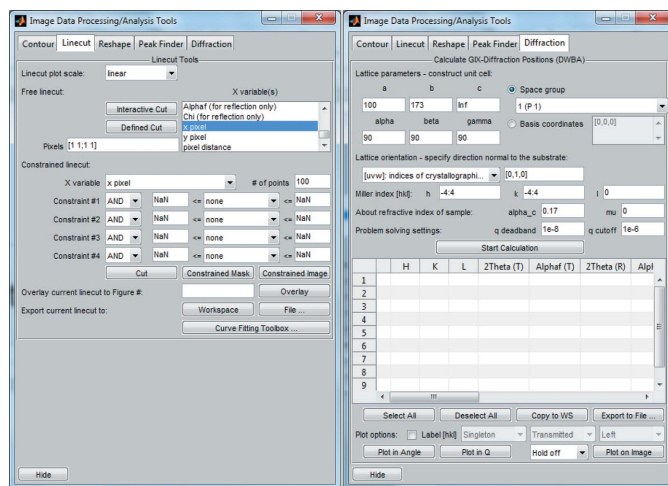


Figure 11
Data processing panels.

APPENDIX B

Screenshots of GIXSGUI

Screenshots of GIXSGUI can be seen in Fig. 10 and Fig. 11. A full list and description of *gixsdata* properties and methods, as well as other functions, can be found in the manual of the toolbox.

Acknowledgements

We express great gratitude to Dr Joseph Strzalka for very helpful discussions and to the users of Sector 8-ID-E for suggestions and input. We also thank Professor Rafael Verduzco for providing the data for Fig. 5, Professor Ting Xu

for providing the data for Fig. 8 and Professor Darren Dunphy for providing the data for Fig. 9. This work and use of the Advanced Photon Source, an Office of Science User Facility operated for the US Department of Energy (DOE) Office of Science by Argonne National Laboratory, was supported by the US DOE under contract No. DE-AC02-06CH11357.

References

- Als-Nielsen, J. & McMorrow, D. (2011). *Elements of Modern X-ray Physics*, 2nd ed. Chichester: Wiley.
- Babonneau, D. (2010). *J. Appl. Cryst.* **43**, 929–936.
- Baker, J. L., Jimison, L. H., Mannsfeld, S., Volkman, S., Yin, S., Subramanian, V., Salleo, A., Alivisatos, A. P. & Toney, M. F. (2010). *Langmuir*, **26**, 9146–9151.
- Breiby, D. W., Bunk, O., Andreasen, J. W., Lemke, H. T. & Nielsen, M. M. (2008). *J. Appl. Cryst.* **41**, 262–271.
- Buerger, M. J. (1940). *Physics*, **26**, 637–642.
- Busch, P., Rauscher, M., Smilgies, D.-M., Posselt, D. & Papadakis, C. M. (2006). *J. Appl. Cryst.* **39**, 433–442.
- Chen, W., Nikiforov, M. P. & Darling, S. B. (2012). *Energy Environ. Sci.* **5**, 8045–8074.
- Chourou, S. T., Sarje, A., Li, X. S., Chan, E. R. & Hexemer, A. (2013). *J. Appl. Cryst.* **46**, 1781–1795.
- Cser, F. (2001). *J. Appl. Polym. Sci.* **80**, 2300–2308.
- Cullity, B. D. & Stock, S. R. (2001). *Elements of X-ray Diffraction*, 3rd ed. London: Prentice Hall International.
- Dunphy, D., Fan, H., Li, X., Wang, J. & Brinker, C. J. (2008). *Langmuir*, **24**, 10575–10578.
- Hailey, A. K., Hiszpanski, A. M., Smilgies, D.-M. & Loo, Y.-L. (2014). *J. Appl. Cryst.* **47**, 2090–2099.
- He, B. B. (2009). *Two-Dimensional X-ray Diffraction*, 1st ed. Hoboken: John Wiley and Sons.
- Jiang, Z., Lee, D. R., Narayanan, S., Wang, J. & Sinha, S. K. (2011). *Phys. Rev. B*, **84**, 075440.
- Jiang, Z., Li, X., Strzalka, J., Sprung, M., Sun, T., Sandy, A. R., Narayanan, S., Lee, D. R. & Wang, J. (2012). *J. Synchrotron Rad.* **19**, 627–636.
- Jiang, Z., Lin, X.-M., Sprung, M., Narayanan, S. & Wang, J. (2010). *Nano Lett.* **10**, 799–803.
- Kao, J., Bai, P., Chuang, V. P., Jiang, Z., Ercius, P. & Xu, T. (2012). *Nano Lett.* **12**, 2610–2618.
- Lazzari, R. (2002). *J. Appl. Cryst.* **35**, 406–421.
- Lee, B., Park, Y.-H., Hwang, Y.-T., Oh, W., Yoon, J. & Ree, M. (2005). *Nat. Mater.* **4**, 147–150.
- Lee, B., Park, I., Yoon, J., Park, S., Kim, J., Kim, K.-W., Chang, T. & Ree, M. (2005). *Macromolecules*, **38**, 4311–4323.
- Liao, H.-C., Tsao, C.-S., Shao, Y.-T., Chang, S.-Y., Huang, Y.-C., Chuang, C.-M., Lin, T.-H., Chen, C.-Y., Su, C.-J., Jeng, U.-S., Chen, Y.-F. & Su, W.-F. (2013). *Energy Environ. Sci.* **6**, 1938–1948.
- Müller-Buschbaum, P. (2014). *Adv. Mater.* **46**, 7692–7709.
- Narayanan, S., Wang, J. & Lin, X.-M. (2004). *Phys. Rev. Lett.* **93**, 135503.
- Parratt, L. G. (1954). *Phys. Rev.* **95**, 359–369.
- Pereira, S., Correia, M. R., Pereira, E., O'Donnell, K. P., Alves, E., Sequeira, A. D., Franco, N., Watson, I. M. & Deatcher, C. J. (2002). *Appl. Phys. Lett.* **80**, 3913–3915.
- Rauscher, M., Paniago, R., Metzger, H., Kovats, Z., Domke, J., Peisl, J., Pfannes, H.-D., Schulze, J. & Eisele, I. (1999). *J. Appl. Phys.* **86**, 6763–6769.
- Renaud, G., Lazzari, R. & Leroy, F. (2009). *Surf. Sci. Rep.* **64**, 255–380.
- Reynolds, R. C. (1986). *Clay Clay Miner.* **34**, 359–367.
- Robach, O., Garreau, Y., Aid, K. & Véron-Jolliot, M. B. (2000). *J. Appl. Cryst.* **33**, 1006–1018.
- Shayduk, R. (2010). *J. Appl. Cryst.* **43**, 1121–1123.
- Sinha, S. K., Sirota, E. B., Garoff, S. & Stanley, H. B. (1988). *Phys. Rev. B*, **38**, 2297–2311.
- Smilgies, D.-M. (2002). *Rev. Sci. Instrum.* **73**, 1706–1710.

- Smilgies, D.-M. (2009). *J. Appl. Cryst.* **42**, 1030–1034.
- Smilgies, D.-M. & Blasini, D. R. (2007). *J. Appl. Cryst.* **40**, 716–718.
- Smilgies, D.-M., Blasini, D. R., Hotta, S. & Yanagi, H. (2005). *J. Synchrotron Rad.* **12**, 807–811.
- Stein, G. E., Kramer, E. J., Li, X. & Wang, J. (2007). *Macromolecules*, **40**, 2453–2460.
- Tate, M. P., Urade, V. N., Kowalski, J. D., Wei, T.-C., Hamilton, B. D., Eggiman, B. W. & Hillhouse, H. W. (2006). *J. Phys. Chem. B*, **110**, 9882–9892.
- Tolan, M. (1999). *X-Ray Scattering from Soft-Matter Thin Films*. Berlin: Springer.
- Vlieg, E. (1997). *J. Appl. Cryst.* **30**, 532–543.
- Vlieg, E. (1998). *J. Appl. Cryst.* **31**, 198–203.
- Wang, J., Bedzyk, M. J. & Caffrey, M. (1992). *Science*, **258**, 775–778.
- Wang, J., Bedzyk, M. J., Penner, T. L. & Caffrey, M. (1991). *Nature*, **354**, 377–380.
- Yoshida, H., Inaba, K. & Sato, N. (2007). *Appl. Phys. Lett.* **90**, 181930.